

Fabrication of TiN-based three-terminal nano mechanical relays using nanoimprint technology

Y. J. Chang · D. Y. Liu · C. L. Kuo

Received: 1 June 2012 / Accepted: 31 July 2012 / Published online: 10 August 2012
© Springer-Verlag 2012

Abstract This paper reports the fabrication of nanoscale mechanical relays using a nanoimprint technology, called contact-transfer and mask-embedded lithography. This cost effective method facilitates the fabrication of nanoscale metallic source electrodes in one easy step. For the design and simulation of relays, we developed a purpose-built system to measure the resonant frequency of TiN nanostructures to determine the mechanical properties of nanoscale thin films. The results presented a Young's modulus of approximately 600 GPa and residual stress low enough to be disregarded in the proposed process. Finally, we succeeded in fabricating three-terminal nano-relays of various lengths, the operation of which was demonstrated by measuring the I–V curve of each device. Measured pull-in voltages were compared with those of the simulation results.

1 Introduction

In accordance with Moore's Law, the past several decades have seen unprecedented improvements in the performance of silicon-based microelectronics, such as integrated circuits (ICs). The necessity for high densities has resulted in the feature size reaching the sub-100 nm scale (ITRS 2005). At such scales, however, the power consumption of ICs increases considerably due to power leakage (Roy et al. 2003).

Nanoelectromechanical systems are considered an effective solution to the problem of power leakage, and nanoscale mechanical relays represent the next generation

of transistors (Pott et al. 2010). Two nanomaterials have been widely employed in the construction of nanoscale mechanical relays: carbon nanotubes (Jang et al. 2005; Lee 2009) and nanowires (Ziegler et al. 2004). Despite their excellent mechanical and electrical properties, the uniformity of these nanomaterials and the associated fabrication processes pose a number of challenges to their further development. The material properties and dimensions of nanotubes and nanowires vary, even within the same fabrication batch, and the fabrication process can be cumbersome (Jang et al. 2005). In addition, the growth of nanotubes in a predefined location is difficult to control. One alternate approach is the "top-down" method, utilizing techniques such as e-beam lithography or focused ion beam lithography (Jang 2008a, b). However, the throughput of these methods is low, rendering them unsuitable for mass production. Nanoimprint technology is considered the next generation nano-fabrication technology for high volume production. It was introduced by Professor S. Y. Chou at Princeton University in 1996 (Chou et al. 1996). This "thermal nanoimprint" technology requires high temperature and high pressure to form patterns on a PMMA polymer layer. Subsequently, two additional nanoimprint technologies have been developed: step and flash imprint lithography (SFIL) (Bailey et al. 2000; Resnick et al. 2005) and soft lithography (Xia and Whitesides 1995; Lahiri et al. 1999). SFIL employs UV-cured epoxy to reduce the pressure and eliminate the heating step required in the thermal nanoimprint process. Soft lithography transfers a polymer layer from molds onto substrates to create patterns. In all of these nanoimprint technologies, polymer patterns are used as a mask to etch consecutive layers. To pattern metallic layers, however, a lift-off process is usually required, which involves the substitution of the polymer mask for a hard mask to compensate for low etching selectivity.

Y. J. Chang (✉) · D. Y. Liu · C. L. Kuo
Department of Mechanical Engineering, National Yunlin
University of Science and Technology, Douliou, Taiwan
e-mail: changy@yuntech.edu.tw

In this study, we employed a novel nanoimprint technology, called contact-transfer and mask embedded lithography (CMEL) to pattern and form TiN-based nano-relays (Lee and Chui 2008). In this process, a hard mask is imprinted directly onto the substrate for patterning. Contact-transfer and mask embedded lithography is simpler than the lift-off process, shows considerable potential for the mass production of nanoscale relays, and is easily integrated into the fabrication of semiconductors.

2 Principles and fabrication process

Figure 1 presents the structure of a nanoscale mechanical relay. This is a clamped–clamped type three-terminal relay, comprising one source, one drain, and two gate electrodes. It is vertically configured; i.e., the source electrode is suspended over the drain and gate electrodes, with the gate electrodes placed symmetrically on both sides of the drain electrode. The mechanical nanorelay is actuated by an electrostatic force generated between the two gates and source electrodes. High voltage is simultaneously applied to the two gate electrodes, while the source electrode is grounded. The relay is normally in an “off” state; it is switched to an “on” state once the suspending source electrode is bent by the electrostatic force to make contact with the drain electrode.

The fabrication process comprises two steps: fabrication of the mold followed by fabrication of the bottom substrate. To fabricate the mold, we first deposited a 300 nm thick silicon dioxide layer on silicon using a wet thermal process. We then patterned the oxide layer using photolithography and wet etching to create submicron features. Next, the silicon substrate was patterned by induced coupled plasma reactive ion etching (ICP-RIE). The etching depth of the silicon substrate was 300 nm. The oxide layer was then completely removed by wet etching. The silicon patterns functioned as molds to define the source electrode during the CMEL step of fabricating the bottom substrate. The next step involved dicing the wafer into $2 \times 2 \text{ cm}^2$

pieces and coating the silicon molds with anti-stiction coatings: 1H, 1H, 2H, 2H-perfluorooctyltrichlorosilane, through vapor deposition. Finally, a 50 nm thick Au layer was deposited by e-beam evaporation to complete the fabrication of the mold.

The process of fabricating the bottom substrate was more complex than that for the mold, as shown in Fig. 2. A 100 nm thick oxide layer was first deposited on the silicon wafers as an insulating layer. A 300 nm thick polysilicon layer was then deposited and patterned to define the area for the drain and gate electrodes. The polysilicon layer in the patterned area was completely removed to expose the oxide layer. We then deposited and patterned a 100 nm thick TiN layer to form the drain and gate electrodes within the patterned area that had been previously defined. After defining the drain and gate electrodes, we deposited a thick oxide layer and performed CMP to obtain a flat upper surface and expose the remainder of the polysilicon layer. A 50 nm thick TiN layer was deposited on the substrate as material for the source electrode. Finally, we applied CMEL to complete the fabrication of the device. The CMEL process is shown in Fig. 3. A layer of A4 950 PMMA was spin-coated onto the bottom substrate. The top Au pattern on the mold contacted the PMMA layer at an air pressure of 2 kgf/cm^2 . Meanwhile, both the bottom substrate and mold were heated to 95°C for 6 min. After cooling, the mold and bottom substrate were separated and the top Au pattern was transferred to the PMMA layer. The Au on the PMMA layer was then used as a mask in RIE to define the source electrode. The RIE process involved two steps: the introduction of oxygen to pattern the PMMA layer and the introduction of SF_6 to pattern the top TiN layer. After removal of the Au mask with acetone, the oxide layer beneath the top TiN layer was removed by buffer oxide etching (BOE). Finally, the fabrication was completed with the application of a CO_2 critical point dryer to prevent the source electrode from stiction.

Throughout the process, the length of the source electrode was defined by the spacing between two polysilicon patterns on the bottom substrate. The source electrodes were successfully fabricated in lengths from 4 to $20 \mu\text{m}$, all with widths of approximately 600 nm.

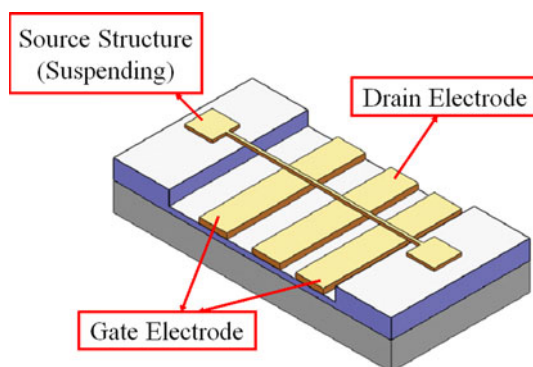
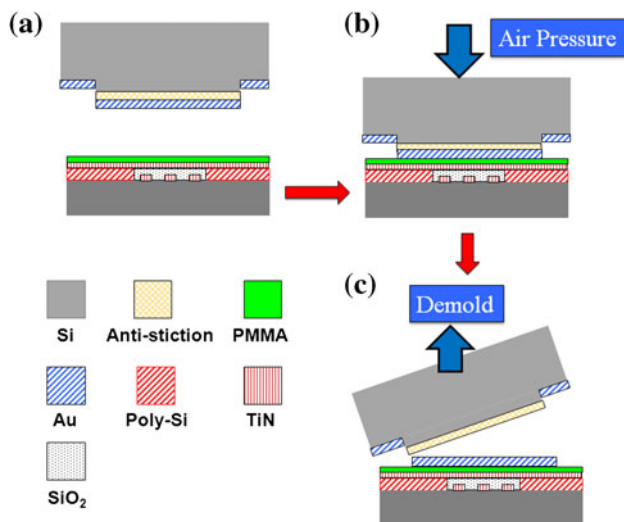
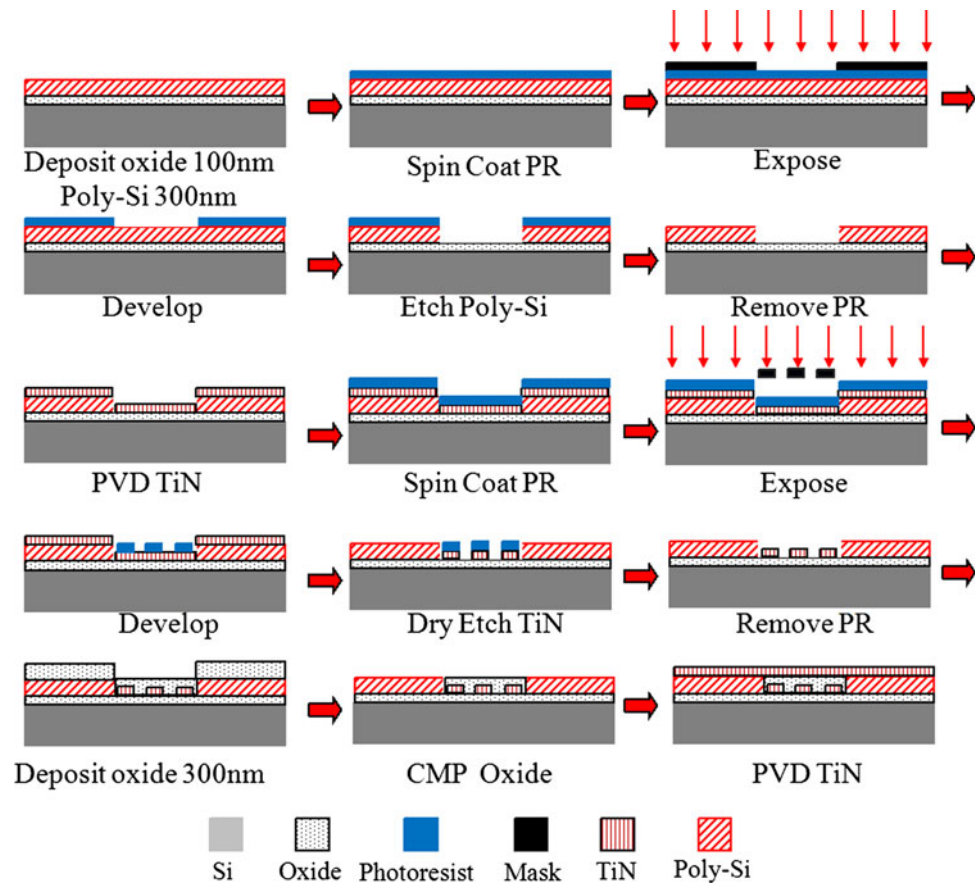


Fig. 1 Structure of a nanoscale mechanical relay

3 Characterization of mechanical properties

To estimate the performance of mechanical nano-relays, the mechanical properties of TiN nanoscale thin film, such as the Young's modulus and residual stress, must be well characterized. This study employed a purpose-built system to measure the resonant frequencies of TiN structures in different modes to determine the mechanical properties of the TiN film.

We fabricated TiN sample structures similar to the source electrodes in the nano-relays for characterization.

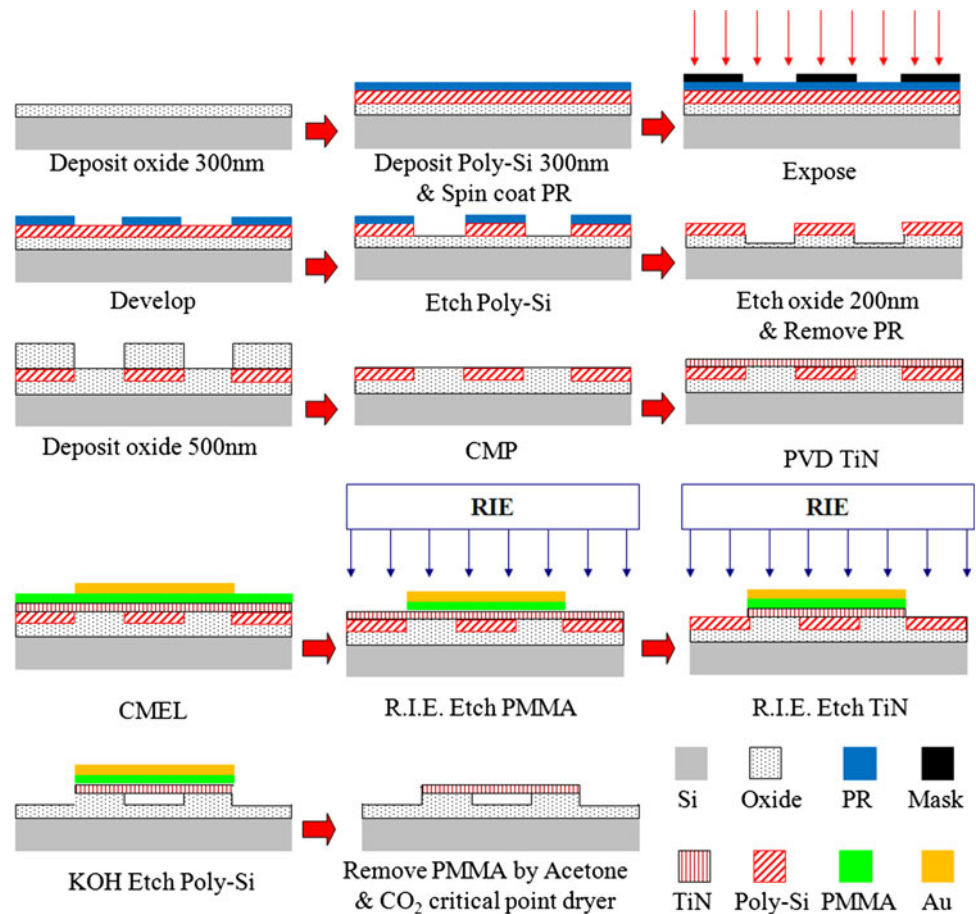
Fig. 2 Fabrication process of bottom substrate**Fig. 3** CMEL process

The sample structures were clamped–clamped type beams, as with the nano-relays, and were fabricated on a 6 in silicon wafer. The fabrication process, shown in Fig. 4, is similar to that described in the previous section, except that we omitted the drain and gate electrode fabrication steps. The length of the sample structures was also longer than the actual relay devices in order to accommodate frequency

measurement capabilities in the system. Three suspended TiN structures of different lengths (300, 400, and 500 μm) were designed to have resonant frequencies in the kHz range. The wafer was then diced into $2 \times 2 \text{ cm}^2$ segments. An example device is shown in Fig. 5. Figure 5a shows an optical image of a sample structure, following the CMEL step. The large pads at the ends of the structure are for the applied voltage. Figure 5b is an SEM image of a successfully suspended TiN structure.

Our measurement system is based on a Michelson interferometer, comprising a commercially available laser interferometer, a lens, a function generator, an oscilloscope, two probes and three translation stages. A schematic diagram of the setup is shown in Fig. 6, while the actual experimental setup is displayed in Fig. 7. The laser interferometer is a fiber-coupled homodyne interferometer (SIOS, MODEL SP2 120, Germany) (Schott 2010) comprising a He–Ne laser source, an optical fiber, a collimator, a reference mirror, a beam splitter and a signal processing unit. The wavelength of the laser is 632.8 nm. The laser was coupled to the fiber and led through the collimator and beam splitter. One laser beam was then reflected by the reference mirror while the other beam was directed toward the sample and reflected back into the interferometer. A $2 \times 2 \text{ cm}^2$ substrate with 96 TiN sample structures was

Fig. 4 Fabrication process of sample structure for frequency measurements



placed on a translation stage perpendicular to the laser beam. Two probes touched a pad on the sample structure and substrate, respectively to supply voltage from the function generator and to actuate the vibration of the sample structure. The interferometer was used to detect the interference between the reflection from both the reference mirror and the sample. When the sample reached its resonant frequencies, the interferometer sensed a displacement jump and an obvious signal change appeared on the oscilloscope. In this manner, the resonant frequencies were identified. A microscope and CCD were used to align the laser beam with the sample and take images of the sample. The system detected various vibration modes, which were used to characterize the Young's modulus and residual stress of the TiN sample structures.

The resonant frequency of a clamped-clamped beam with a residual stress can be expressed as (Blevins 1993):

$$\frac{\langle w_i |_{N \neq 0} \rangle}{\langle w_i |_{N=0} \rangle} = 1 + \frac{N}{N_b} \frac{\lambda_i^2}{\lambda_i^2} \quad (1)$$

where $\langle w_i |_{N \neq 0} \rangle$ is the resonant frequency with existing residual stress; i is the vibration mode; N is the force acting on the cross-section area due to residual stress; N_b is the buckling load, expressed as:

$$N_b = \frac{4\pi^2 EI}{L^2} \quad (2)$$

where E is the Young's modulus of the material, I is area moment of inertia, L is the length of the structure. $\langle w_i |_{N=0} \rangle$ is the resonant frequency without residual stress, expressed as:

$$\langle w_i |_{N=0} \rangle = \frac{\lambda_i^2}{L^2} \left(\frac{EI}{\rho A} \right)^{1/2} \quad (3)$$

where ρ is the density of the material; A is the cross-sectional area of the structure. λ_i is the coefficient corresponding to the resonance modes listed in Table 1.

Three $2 \times 2 \text{ cm}^2$ segments on the far-left (FL), middle, and far-right (FR) of the wafers were selected for characterization. Each segment included devices of three different lengths. For each length, we measured the resonant frequency of one device in the far-left and far-right segments and measured that of three devices in the middle segment. For each device, we measured the first five resonant modes. The measured resonant frequencies of all sample devices are listed in Table 2. By varying the Young's modulus and residual stress, we determined the best fit for each device. The mechanical properties of the TiN thin film were then

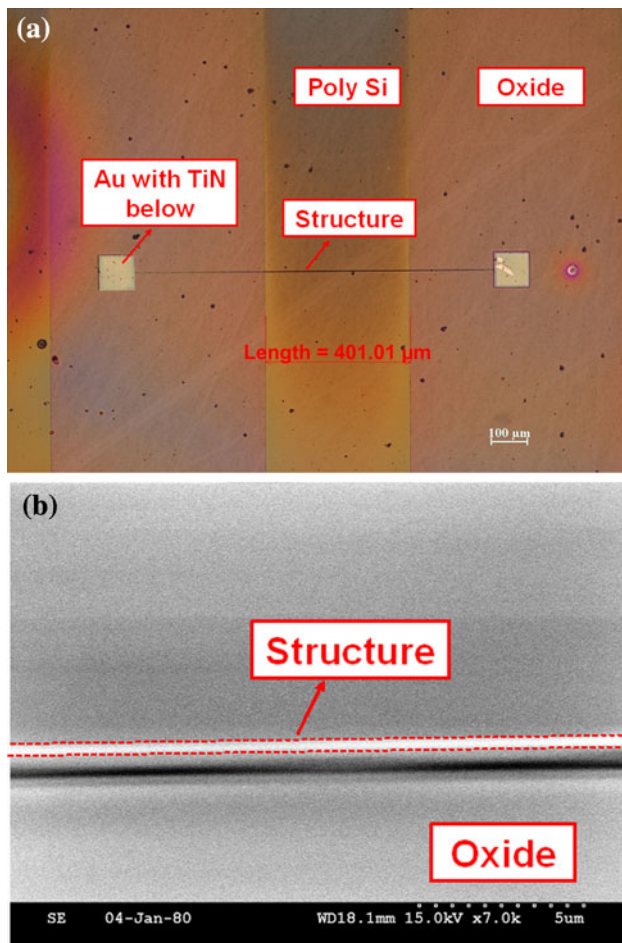


Fig. 5 Pictures of a sample device for material properties characterization. **a** OM image of a sample with 400 μm in length after CMEL. **b** SEM picture of a suspending TiN structure

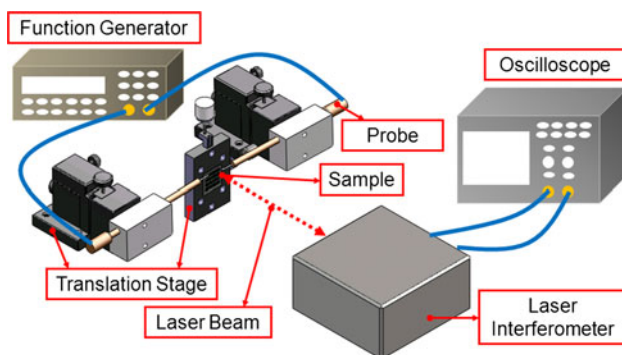


Fig. 6 Schematics of experimental setup

extracted using Eq. (1), an example of which is shown in Fig. 8. The same technique was then applied to other devices. The Young's modulus and residual stresses of all devices are listed in Table 3 and Fig. 9.

The Young's Modulus is in the range of 526 GPa and 633 GPa, with an average of 592 GPa. The residual stress

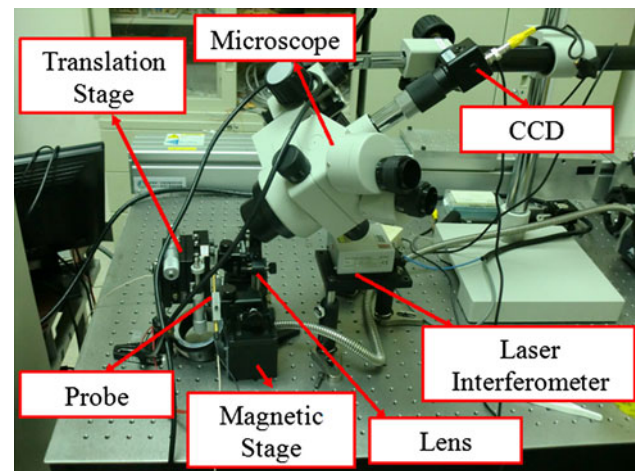


Fig. 7 Picture of experimental setup

Table 1 Coefficients of different resonance modes

Mode (<i>i</i>)	λ_i
0	22.37
1	61.672
2	120.903
3	199.859
4	298.556

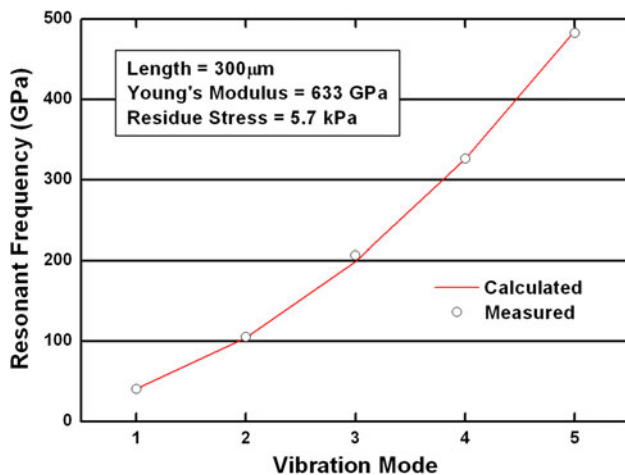
is in the range of 5.7 to 22.3 kPa, which was considered too small for consideration in the simulation of the pull-in voltage of nano-relays in the following section.

4 Simulations

The simulation of pull-in voltage for nanorelays of various lengths was performed using COMSOLTM multiphysics. The geometry of the devices in the simulation matched that of the fabricated devices listed in Table 4. The simulation was performed in two-dimensions only. The Young's Modulus of TiN was set to 600 GPa and the structures had no residual stress. From the characterization of the mechanical properties in the previous section, we deemed the above setting to be reasonable. The thickness of the source electrode was only 50 nm, divided into eight elements. The aspect ratio of the mesh element was maintained at 2:1 to ensure excellent meshing quality. The suspended source electrode was the only moving object, both ends of which were fixed, leaving the rest of the source electrode free. The spacing of 100 nm between the source electrode and the bottom electrodes (i.e., drain electrode and gate electrodes) was set as air in the simulation. One of the pull-in simulation results is shown in Fig. 10. The color shows the displacement in the *y*

Table 2 Measured resonant frequency of sample devices at different modes

No.	Position	Length (μm)	Resonant frequency of different modes (kHz)				
			0	1	2	3	4
1	Middle	300	40.44	105.35	206.35	325.95	482.40
2	Middle	300	47.99	107.68	206.45	330.10	485.90
3	Middle	300	43.75	105.65	209.85	327.35	485.35
4	FR	300	53	109	214	332.55	485.85
5	FL	300	50.68	106.50	213.55	329.55	485.50
6	Middle	400	25.32	62.85	106.83	181.75	265.78
7	Middle	400	29.10	64.65	111.45	187.35	270.40
8	Middle	400	27.50	63.55	109.35	185.9	268.3
9	FR	400	28.85	62.50	110.35	186.5	267
10	FL	400	27.40	62.73	110	190.52	271.30
11	Middle	500	20.12	41.73	69.78	121.20	170.92
12	Middle	500	21	39.50	71.80	129.40	175.10
13	Middle	500	20.28	43	71.80	120.80	175.10
14	FR	500	22.80	48.45	70.50	122.35	175.25
15	FL	500	23.12	44.75	73.7	124.35	169

**Fig. 8** A fitting curve to the measured resonant frequency. The device is 300 μm in length and the frequencies are fitted by varying Young's modulus and residual stress

direction (i.e., normal to the source electrode). The pull-in voltage was 89 V, as shown in Fig. 10. The pull-in simulation results of all devices are listed in Table 4 and shown in Fig. 11.

5 Results and discussion

This study successfully fabricated devices of various lengths. An SEM image of a 5 μm long device is shown in Fig. 12. The width of all the fabricated devices was 663 nm, while the variation in length was controlled to within 0.7 μm .

Table 3 Calculated Young's modulus and residual stresses by fitting the frequency measurements

No.	Position	Length (μm)	E (GPa)	Residual stress (kPa)
1	Middle	300	633	5.7
2	Middle	300	615	15.8
3	Middle	300	624	10.2
4	FR	300	606	22.33
5	FL	300	606	19.4
6	Middle	400	586	7.2
7	Middle	400	614	11.6
8	Middle	400	587	9.9
9	FR	400	603	9.57
10	FL	400	574	11.7
11	Middle	500	562	9.6
12	Middle	500	587	10.5
13	Middle	500	593	9.6
14	FR	500	575	12.8
15	FL	500	526	13.2

The pull-in voltage of the devices was characterized by measuring the I–V curves of each device using a probe station with a semiconductor parameter analyzer. Actuation voltage was simultaneously applied to two gate electrodes while the source electrode was grounded. The increment of actuation voltage was 0.1 V. At the same time, a small voltage of 50 mV was applied to the drain electrode. Once the pull-in voltage was reached, a sudden change in current

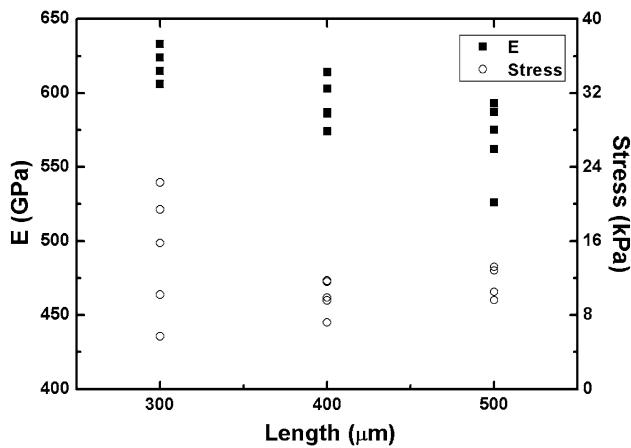


Fig. 9 Distributed Young's modulus and residue stress of devices. Solid square denotes Young's modulus while open circle denotes residual stresses

could be detected and an ohmic contact between the source and drain electrodes was formed.

The I–V measurement results of nanorelays with different lengths are shown in Figs. 13, 14, 15, 16. The lengths of the devices in each figure are 4, 5, 8, and 20 μm , respectively. A sudden increase of drain current (i.e., IDS) from few nano-ampere to micro-ampere was used to determine the pull-in phenomenon. The measured pull-in voltages were 16.6, 12, 4, and 1.75 V, respectively. After the occurrence of pull-in, an ohmic contact was easily observed from the linear relationship in the I–V curve. The contact resistance of 4 and 5 μm devices was 30 k Ω , while the contact resistances of 8 and 20 μm devices were 6.67

Table 4 List of geometry of simulated devices

Length of S (μm)	Width of D (nm)	Width of G (nm)	Spacing b/w D and G (nm)	Pull-in voltage (Volt)
4	800	600	500	89
5	800	600	500	47
8	800	600	500	28
10	2,000	3,000	500	16.2
20	2,000	3,000	500	6.6
40	2,000	3,000	500	1.4

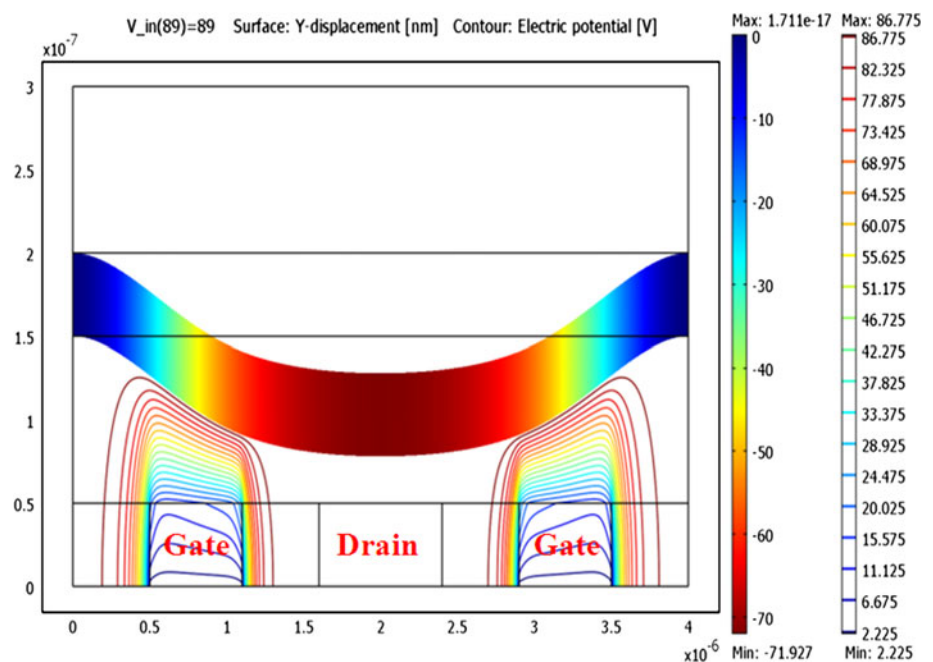
S source, D drain, G gate, b/w between

and 2.3 k Ω , respectively. The difference in contact resistance of the devices was due mainly to the contact area between the source and drain electrodes. A longer source electrode resulted in a larger contact area from the source to the drain electrodes when the pull-in phenomenon occurred.

A comparison of measured and simulation results is shown in Fig. 17, clearly illustrating that the measured pull-in voltages were all smaller than those in the simulation. Three factors are considered to be the cause:

1. The BOE used in the process was able to etch the TiN slightly, with an etching rate of approximately 2.5 nm/min in BOE (William et al. 2003). A thinner structure would result in a smaller pull-in voltage.
2. The air gap was determined by the CMP step in the fabrication process and the variation of air gap could not be well controlled.

Fig. 10 Pull-in voltage simulation of a 4 μm long relay



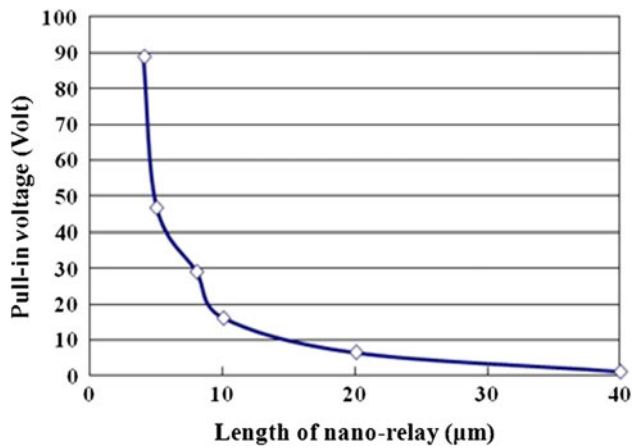


Fig. 11 Simulation results of pull-in voltage with different lengths of nano mechanical relays

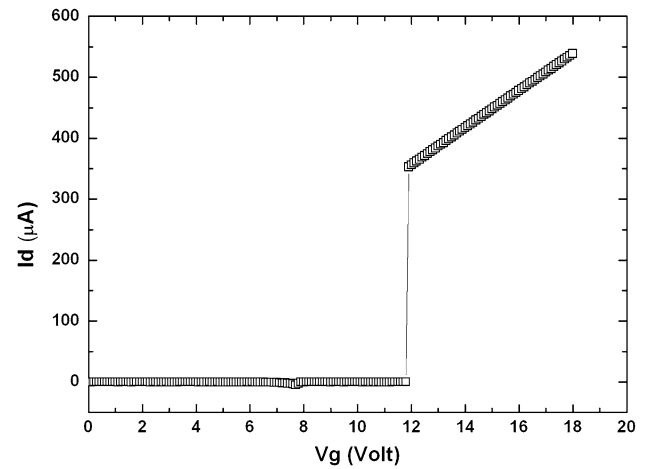


Fig. 14 Curve of a fabricated 5 μm long relay

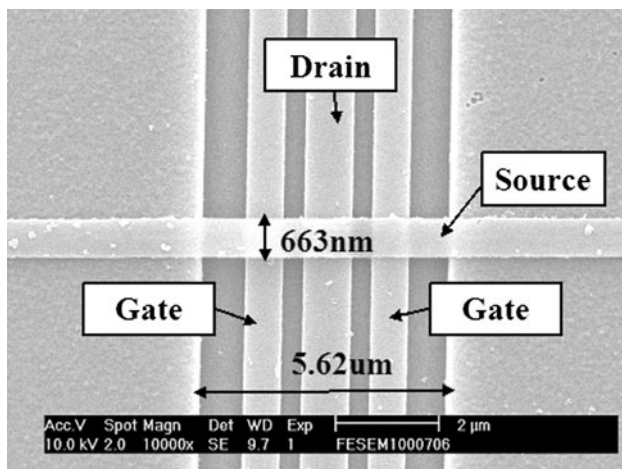


Fig. 12 SEM picture of a fabricated 5 μm long relay

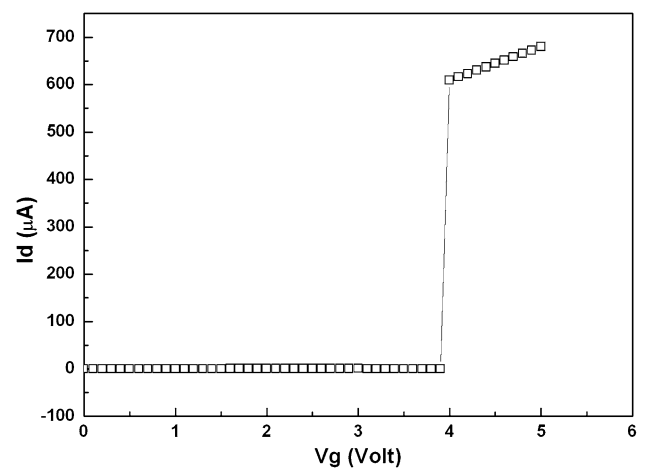


Fig. 15 Curve of a fabricated 8 μm long relay

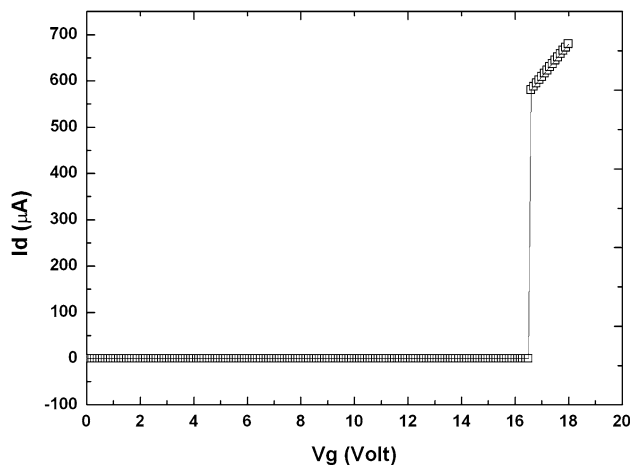


Fig. 13 Curve of a fabricated 4 μm long relay

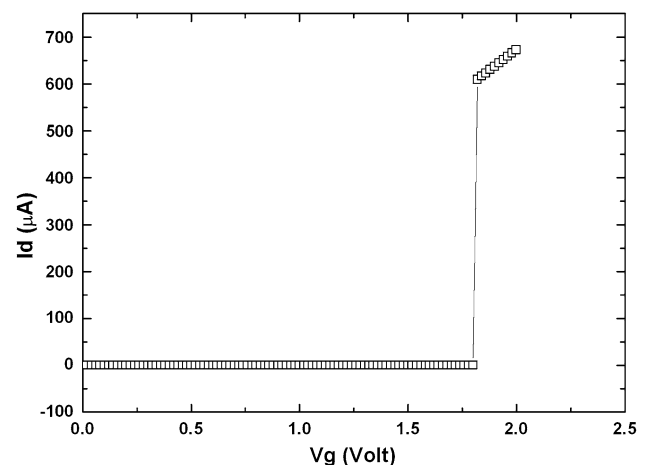


Fig. 16 Curve of a fabricated 20 μm long relay

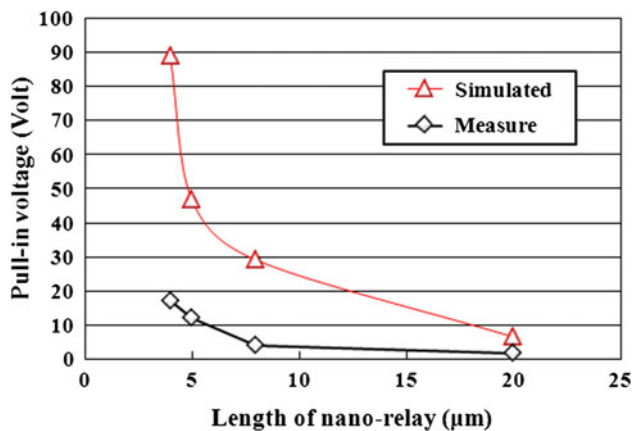


Fig. 17 Comparison of pull-in voltage between the simulated and measured results

3. A source electrode, 50 nm thick, moved approximately 100 nm when pulled in, which may have led to plastic deformation resulting in a reduced pull-in voltage.

6 Conclusion

This study successfully applied nanoimprint technology to the fabrication of nanoscale TiN-based mechanical relays. The Young's modulus and residual stress of the TiN layer were extracted from the measurements of resonant frequency in TiN structures. The results show a Young's modulus of approximately 600 GPa and negligible residual stress in the TiN layer. The relays were demonstrated by measuring the I–V curves, and the pull-in voltages ranged from 16 to 1.75 V, depending on length. An ohmic contact was formed between the source and drain electrodes, demonstrating a successful relay operation. We then compared the simulated pull-in voltage with the measured results. The measured pull-in voltages were all smaller than the simulated values. We believe that plastic deformation of TiN nano-relays is the main reason for the difference.

Acknowledgments The authors would like to thank the National Science Council (NSC98-2218-E-224-009-) for their financial support and the National Nano-Device Laboratory for supplying equipment,

as well as the Center for Micro/Nano Science and Technology at National Cheng Kung University, Taiwan.

References

- Bailey T, Choi BJ, Colburn M, Meissl M, Shaya S, Ekerdt JG, Sreenivasan SV, Willson CG (2000) Step and flash imprint lithography: template surface treatment and defect analysis. *J Vac Sci Tech B* 18:3572–3577
- Blevins RD (1993) Formulas for natural frequency and mode shape. Kreiger, Florida
- Chou SY, Krauss PR, Renstrom PJ (1996) Nanoimprint lithography. *J Vac Sci Tech B* 14:4129–4133
- ITRS (2005) Emerging research devices. ITRS. <http://www.itrs.net/Links/2005ITRS/>
- Jang WW (2008a) NEMS switch with 30 nm thick beam and 20 nm thick air-gap for high density non-volatile memory applications. *Solid-State Electron* 52:1578–1583
- Jang WW (2008b) Fabrication and characterization of a nanoelectromechanical switch with 15-nm thick suspension air gap. *Appl Phys Lett* 92:103110
- Jang JE, Cha SN, Choi Y, Amaratunga GAJ, Kang DJ, Hasko DG, Jung JE, Kim KM (2005) Nanoelectromechanical switches with vertically aligned carbon nanotubes. *Appl Phys Lett* 87:113102
- Lahiri J, Ostuni E, Whitesides GM (1999) Patterning ligands on reactive SAMs by microcontact printing. *Langmuir* 15:2055–2060
- Lee SW (2009) Carbon-nanotube based nano electromechanical switches. *J Korean Phys Soc* 55:957–961
- Lee YC, Chui CY (2008) Micro-/nano-lithography on the contact transfer of thin film and mask embedded etching. *J Micromech Microeng* 18:075013
- Pott V, Kam H, Nathanael R, Jeon J, Alon E, Liu TJK (2010) Mechanical computing redux: relays for integrated circuit applications. *Proc IEEE* 98:2076–2094
- Resnick DJ, Sreenivasan SV, Willson CG (2005) Step and flash imprint lithography. *Mater Today* 8(2):34–42
- Roy K, Mukhopadhyay S, Mahmoodi-Meimand H (2003) Leakage current mechanisms and leakage reduction techniques in deep-submicrometer CMOS circuits. *Proc IEEE* 91:305–327
- Schott W (2010) Developments in homodyne interferometry. *Key Eng Mater* 437:84–88
- William KR, Gupta K, Wasilik M (2003) Etch rates for micromachining processing—part II. *J Microelectromech Syst* 12:761–778
- Xia Y, Whitesides GM (1995) Reduction in the size of features of patterned SAMs generated by microcontact printing with mechanical compression of the stamp. *J Adv Mater* 7:471–473
- Ziegler KJ, Lyons DM, Holmes JD, Ertz D, Polyakov B, Olin H, Svensson K, Olsson E (2004) Bistable nanoelectromechanical devices. *Appl Phys Lett* 84:4074–4076